Direct Experimental Evidence for Dissociative Photoionization of Oxygen Molecule via 2 Σ u − Ionic "Optical Dark" State

6 AUTHORS, INCLUDING:

Xiaofeng Tang
Hefei Institute of Physical Sciences, Chinese A…
27 PUBLICATIONS   112 CITATIONS

SEE PROFILE

Xiaoguo Zhou
University of Science and Technology of China
51 PUBLICATIONS   317 CITATIONS

SEE PROFILE

Shilin Liu
University of Science and Technology of China
103 PUBLICATIONS   698 CITATIONS

SEE PROFILE

Article

Direct Experimental Evidence for Dissociative Photoionization of Oxygen Molecule via $^2\Sigma_u^-$ Ionic "Optical Dark" State

Xiaofeng Tang,[†,‡] Xiaoguo Zhou,*[,†] Manman Wu,[†] Yu Cai,[†] Shilin Liu,[†] and Liusi Sheng[‡]

[†]Hefei National Laboratory for Physical Sciences at the Microscale, Department of Chemical Physics, University of Science and Technology of China, Hefei, Anhui 230026, China

[‡]National Synchrotron Radiation Laboratory, University of Science and Technology of China, Hefei, Anhui 230029, China

ABSTRACT: Direct experimental evidence for dissociative photoionization of oxygen molecule via the $^2\Sigma_u^-$ ionic optical dark state is presented by an investigation using the method of threshold photoelectron−photoion coincidence (TPEPICO) velocity imaging. Besides vibrational progress of the $B^2\Sigma_g^-$ state, several weak vibrational bands of the $^2\Sigma_u^-$ ionic optical dark state are observed concomitantly in an excitation energy range of 20.2−21.1 eV. Only O^+ fragments are detected in the whole excitation energy range; therefore, all vibrational bands are completely predissociative. TPEPICO three-dimensional time-sliced velocity images of O^+ fragments dissociated from vibrational state-selected $O_2^+(^2\Sigma_u^-, v^+)$ ions are recorded. For the $^2\Sigma_u^-(v^+=0-3)$ vibrational states, only the lowest dissociation channel of $O^+(^4S) + O(^3P)$ is observed. Once the photon energy is slightly increased to the $^2\Sigma_u^-(v^+=4)$ level, a new concentric doughnut appears in the image, indicating that the second dissociation channel of $O^+(^4S) + O(^1D)$ is identified indeed. With the aid of potential energy curves, the dissociative mechanism of O_2^+ in the $^2\Sigma_u^-(v^+)$ state is proposed.
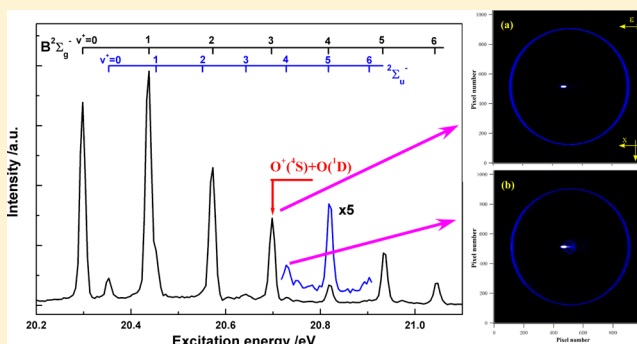
1. INTRODUCTION

By measuring zero-kinetic-energy electrons and their corresponding ions in photoionization, threshold photoelectron−photoion coincidence (TPEPICO) is a powerful experimental technique to investigate dissociation dynamics of state-selected ions.[1−5] As synchrotron radiation (SR) can provide high-flux vacuum ultraviolet (VUV) photons, it has been extensively used as a light source in TPEPICO experiments.[6−10] Recently, employing a double velocity map imaging (VMI) design for collecting photoelectrons and photoions simultaneously, TPEPICO velocity imaging has been developed to directly measure kinetic energy and angular distributions of fragments dissociated from state-selected ions.[11−13] Because VMI can provide a better kinetic energy resolution than that from fitting the time-of-flight (TOF) profile of fragment ions,[14,15] some delicate mechanism of dissociation can be revealed.[16−20]

The oxygen molecule and ion are the most significant species on earth and are involved in many gas-phase chemical reactions. As a simple diatomic molecule, the oxygen molecule in the ground state has an electronic configuration of $(1\sigma_g)^2(1\sigma_u)^2(2\sigma_g)^2(2\sigma_u)^2(3\sigma_g)^2(1\pi_u)^4(1\pi_g)^2$. Thus, the O_2^+ ions in various ionic states can be produced by removing an electron from the outer orbits. In the previous photoelectron spectrum[21] and threshold photoelectron spectra (TPES)[22−26] of O_2, most of the ionic states were observed and assigned. Subsequently, many experimental investigations, for example, photoelectron−photoion coincidence (PEPICO),[27−29] TPEPICO,[30−32] and vector correlation,[33] were performed to explore

the dissociation of O_2^+ ions in different ionic states. Only two dissociation channels of O_2^+ ions can be observed below 22 eV; the lowest dissociation limit of $O^+(^4S) + O(^3P)$ is located at 18.733 eV, and the second limit of $O^+(^4S) + O(^1D)$ is 20.700 eV.

In the photon energy range of less than 22 eV, many previous investigations were focused on dissociation of the $B^2\Sigma_g^-$ ionic state. Both the lowest and second dissociation channels were detected for the $v^+ = 4$ and 6 vibrational states of $B^2\Sigma_g^-$, while the second channel of $O^+(^4S) + O(^1D)$ was not observed for the $B^2\Sigma_g^-(v^+=5)$ level yet.[32] The phenomenon was difficult to explain just using the interaction of $B^2\Sigma_g^-$ and nearby ionic states. With the aid of the calculated potential energy curves, a new intersection mechanism has been proposed recently for dissociative photoionization (DPI) of O_2 via the $B^2\Sigma_g^-$ state.[17] At 20.817 eV, both $B^2\Sigma_g^-(v^+=4)$ and concomitant $^2\Sigma_u^-(v^+=5)$ vibrational states are populated simultaneously, and the observed O^+ fragments from the second dissociation channel are produced in predissociation caused by the coupling between $^2\Sigma_u^-(v^+=5)$ and nearby $2^4\Pi_u$ states. When the excitation energy is increased to the $B^2\Sigma_g^-(v^+=5)$ level, the incidental degeneration between it and $^2\Sigma_u^-$ does not exist, and the second dissociation cannot be observed because the energy is lower than the intersection of

the $B^2\Sigma_g^-$ and $2^4\Pi_g$ states. Therefore, the $^2\Sigma_u^-$ state is expected to play a significant role in dissociation of O_2^+ within the excitation energy range.

Due to the forbidden transition for O_2^+, $^2\Sigma_u^-$ is a typical "optical dark" state. Thus, it is very difficult to investigate its dissociation dynamics via photoexcitation from the ionic ground state of gerade symmetry. Fortunately, the ionic states of ungerade symmetry can be probably produced in the TPEPICO experiment through photoexcitation from the ground state of a neutral molecule. A vibrational progression, $v^+ = 0-7$, of $^2\Sigma_u^-$ was observed and assigned, although the intensities were very weak.[17,26] However, direct experimental investigations of DPI of O_2 via the $^2\Sigma_u^-$ ionic state have never been performed until now, and hence, some mysteries in dissociation of the $^2\Sigma_u^-$ state are still kept. These include the following: Can the $^2\Sigma_u^-$ state predissociate indeed along both dissociation channels? What is its predissociation mechanism? What is the branching ratio of O^+ dissociated from the $B^2\Sigma_g^-(v^+=4)$ and $^2\Sigma_u^-(v^+=5)$ states at 20.817 eV? Moreover, although theoretical calculations[34,35] suggested that the intersection of $^2\Sigma_u^-(v^+=5)$ and nearby $2^4\Pi_u$ states was lower than the dissociation limit of $O^+(^4S) + O(^1D)$, direct experimental evidence is lacking. In this work, dissociation of vibrational state-selected $O_2^+(^2\Sigma_u^-,v^+=0-6)$ ions has been studied using the TPEPICO velocity imaging technique. From both obtained speed and angular distributions of O^+ fragments, direct experimental evidence for DPI of O_2 via the $^2\Sigma_u^-$ ionic optical dark state will be shown, and moreover, a potential predissociation mechanism of $O_2^+(^2\Sigma_u^-)$ will be proposed.

2. EXPERIMENTS

All experiments were performed at the U14-A beamline of the National Synchrotron Radiation Laboratory, Hefei, China. The details of the beamline[36] and TPEPICO velocity imaging spectrometer[11] have been introduced previously, and thus, only a brief description is presented here.

Synchrotron radiation from an undulator was dispersed with a 6 m monochromator equipped with a 370 grooves·mm^{-1} spherical grating, which covered a photon energy range of 7.5–22.5 eV. Both entrance and exit slits of the monochromator were set at 80 μm in experiments, and the corresponding resolved power ($E/\Delta E$) of photon energy was about 2000. The absolute photon energy scale of the grating was calibrated using several well-known ionization energies of inert gases, for example, Ar, Kr, and Xe.

Due to the weak intensity of the $O_2^+(^2\Sigma_u^-)$ band, pure O_2 gas (99.99%) without dilution was used in experiments. A continuous supersonic molecular beam (MB) was produced through a 30 μm diameter nozzle with a stagnation pressure of 3 atm and collimated by a 0.5 mm diameter skimmer. In the photoionization region, MB intersected with synchrotron radiation at 10 cm downstream from the nozzle. The source and ionization chambers were pumped, respectively, by 1800 and 1600 L·s^{-1} turbo pumps, where the typical backing pressures were 6×10^{-3} and 5×10^{-5} Pa with MB on, respectively.

Electrons and ions produced in the photoionization processes were pushed apart by the same dc electronic field, and both of their velocity images were mapped simultaneously in the opposite directions. In the double velocity map imaging, electron images were amplified by a repelling electronic field, and a mask with a 1 mm diameter central hole located at the

front of electron detector was utilized to collect zero-kinetic-energy electrons. Thus, nearly all contamination of hot electrons could be suppressed in TPES. Using threshold photoelectrons as starting signals for ion timing, the coincident ions were accelerated and projected onto a dual microchannel plate (MCP) backed by a phosphor screen (Burle Industries, P20). In order to measure a coincident image of target ions, a pulsed high voltage was applied to the MCPs as a mass gate[14,37] when the target ions arrived, whose duration could be adjusted from 60 ns to dc. A TE-cooling CCD detector (Andor, DU934N-BV) was used to record ion images on the screen.

3. RESULTS AND DISCUSSION

3.1. Threshold Photoelectron Spectrum of O_2.
Restricted by the energy resolution of the beamline, the present energy resolution of TPES is about 9 meV (full width at half-magnitude, fwhm).[11] TPES of O_2 in the excitation energy range of 20.2–21.1 eV is recorded and shown in Figure 1,
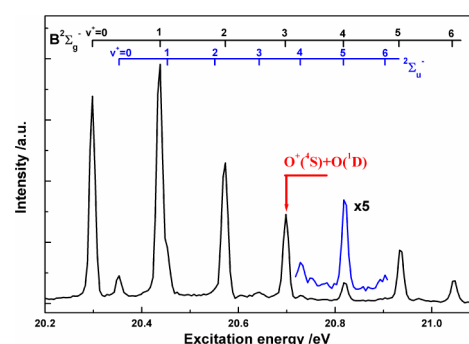

Figure 1. Threshold photoelectron spectrum of O_2 in the excitation energy range of 20.2–21.1 eV. The arrow indicates the dissociation limit of the $O^+(^4S) + O(^1D)$ channel at 20.700 eV.

where two vibrational progresses are clearly observed. As the previous spectra assigned,[23,24,26] the series of vibrational peaks in Figure 1 with the stronger intensity are assigned as the $v^+ = 0-6$ vibrational bands of the $B^2\Sigma_g^-$ ionic state, while the weak progress is contributed by the $^2\Sigma_u^-(v^+=0-6)$ ionic optical dark state. In addition, the $^2\Sigma_u^-(v^+=1,2)$ and $B^2\Sigma_g^-(v^+=1,2)$ vibrational bands overlap partially, and more seriously, the $^2\Sigma_u^-(v^+=5)$ and $B^2\Sigma_g^-(v^+=4)$ bands almost resonate at 20.817 eV. Only $^2\Sigma_u^-(v^+=0, 3, 4, 6)$ vibrational bands can be distinguished independently, where their resonance energies are measured as 20.353, 20.638, 20.727, and 20.897 eV, respectively.

3.2. TPEPICO Velocity Map Image of the O^+ Fragment.
3.2.1. Dissociation of the $O_2^+(^2\Sigma_u^-,v^+=0)$ Ion at 20.353 eV. At 20.353 eV, only the lowest dissociation limit of $O^+(^4S) + O(^3P)$ can be achieved. As shown in the TPEPICO TOF mass spectrum of Figure 2a, only O^+ fragments dissociated from the $O_2^+(^2\Sigma_u^-,v^+=0)$ ions are observed, while no TOF peak for O_2^+ ions can be identified. Therefore, the $^2\Sigma_u^-(v^+=0)$ state of O_2^+ is completely dissociative, like the nearby $B^2\Sigma_g^-$ ionic state. In addition, the TOF profile of O^+ fragments in Figure 2a is obviously broadened, which indicates that a large kinetic energy has been released in dissociation.

The three-dimensional (3D) time-sliced TPEPICO velocity map image of O^+ dissociated from the $O_2^+(^2\Sigma_u^-,v^+=0)$ ion is recorded and shown in Figure 3a. Synchrotron radiation propagates along the y-axis, and the electric vector ε of the photon is along the x-axis. An outer ring with a big diameter is
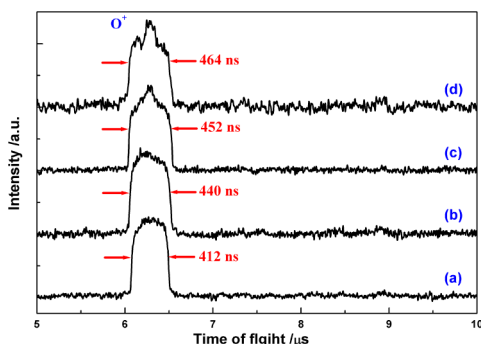
Figure 2. TPEPICO TOF mass spectra for the dissociative photoionization process of O_2 via the $^2\Sigma_u^-$ ionic state at (a) 20.353 ($v^+ = 0$), (b) 20.727 ($v^+ = 4$), (c) 20.817 ($v^+ = 5$), and (d) 20.897 eV ($v^+ = 6$).

observed in the image, in addition to an eccentric bright elliptical spot correlated with the false coincident ions. Because MB flew along the x-axis direction from right to left and the TOF axis was perpendicular to MB, the velocity spread of the beam inevitably caused raw images broadened along the MB direction, as shown in the raw image of Figure 3a. Therefore, the real image needed to be handled prior to extracting speed and angular distributions through a multistep data reduction scheme including subtracting the false coincident events and deconvolution. Its details have been described in refs 16−18. Thus, the modified image of O^+ dissociated from the $O_2^+(^2\Sigma_u^-,v^+=0)$ ion at 20.353 eV is shown in Figure 3b. Only a ring is observed in the image and is contributed to by the $O^+(^4S)$ fragments with the released kinetic energy.

In addition, a very similar image of O^+ fragments is recorded for dissociation of $O_2^+(^2\Sigma_u^-,v^+=3)$ ions because its resonance energy is lower than the second dissociation limit of $O^+(^4S) + O(^1D)$ as well.

3.2.2. Dissociation of the $O_2^+(^2\Sigma_u^-,v^+=4)$ Ion at 20.727 eV. As shown in Figure 1, the resonance energy of the $B^2\Sigma_g^-(v^+=3)$ band is 20.697 eV, which is very close to the $O^+(^4S) + O(^1D)$ dissociation limit of 20.700 eV. Their energy difference is only 3 meV and lower than the TPES uncertainty (∼9 meV); thus, the $O^+(^4S) + O(^1D)$ dissociation channel should probably be observed. The raw 3D time-sliced coincidence image of O^+ recorded at 20.697 eV is shown in Figure 4a. Only an outer ring similar to that in Figure 3a is observed in the image, in addition

to an eccentric bright elliptical spot correlated with the false coincident ions. Therefore, the quantum yield for production of the lowest channel greatly exceeds that of the second channel, and the $O^+(^4S) + O(^1D)$ products are not observed yet.

Once the photon energy is slightly increased to 20.727 eV, the $O_2^+(^2\Sigma_u^-,v^+=4)$ ions are produced and subsequently dissociate. As the excitation energy is higher than its dissociation limit, the second channel of $O^+(^4S) + O(^1D)$ should be observed. However, it is difficult to identify a new weak component superimposed on the center of the wide TOF profile of O^+ in Figure 2b.

The raw 3D time-sliced image of O^+ dissociated from $O_2^+(^2\Sigma_u^-,v^+=4)$ ions is recorded and presented in Figure 4b, and its center part has been magnified in Figure 4c. Different from Figure 4a, an additional weak doughnut obviously exists close to the center of the image and concentric with the outer ring. As mentioned above, the outer ring is contributed by O^+ dissociated along the lowest pathway of $O^+(^4S) + O(^3P)$, and hence, the inner doughnut correlates with the $O^+(^4S) + O(^1D)$ channel. Therefore, the new doughnut is definitely direct experimental evidence for the appearance of the $O^+(^4S) + O(^1D)$ channel at 20.727 eV. Comparing both images a and b of Figure 4, the different dissociative mechanisms of the $^2\Sigma_u^-(v^+=4)$ and $B^2\Sigma_g^-(v^+=3)$ states are expected, although their resonance energies are very close.

From Figure 4b, a brief conclusion can be drawn that the most of the $O_2^+(^2\Sigma_u^-,v^+=4)$ ions dissociate along the lowest channel of $O^+(^4S) + O(^3P)$. In principle, the branching ratio of two dissociation channels can be exactly calculated from the accumulated intensity of the image. However, the total kinetic energy released in dissociation of $O_2^+(^2\Sigma_u^-,v^+=4)$ along the $O^+(^4S) + O(^1D)$ channel is only 27 meV, and thus, the corresponding component of the TOF profile of the O^+ fragments is only expanded a little bit. As the 60 ns mass gate for recording the time-sliced image in the experiments is too wide to slice the Newton sphere of $O^+(^4S)$ ions with only 13.5 meV kinetic energy, the center part in the image of Figure 4b looks like a doughnut instead of a ringlet. Thus, it cannot exactly reflect a 3D distribution of O^+ fragment ions yet.

3.2.3. Dissociation of the $O_2^+(^2\Sigma_u^-,v^+=5)$ Ion at 20.817 eV. As shown in Figure 2c, two components are clearly observed in the TOF profile of O^+ fragments at 20.817 eV, and both of their widths are expanded to a certain extent compared with those at 20.727 eV. The modified TPEPICO 3D time-sliced image of
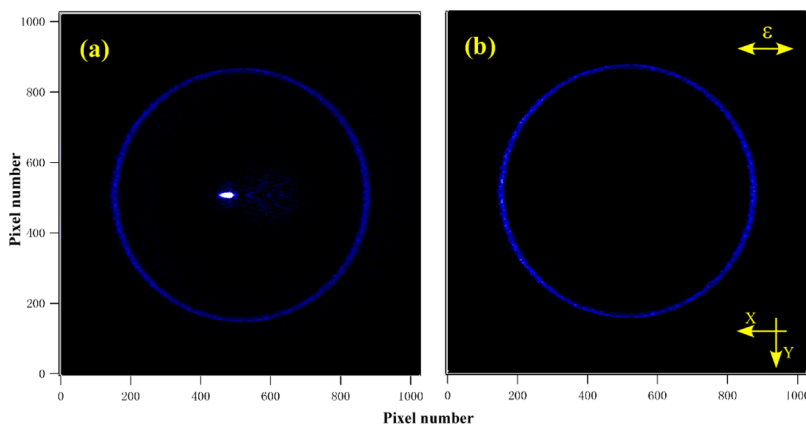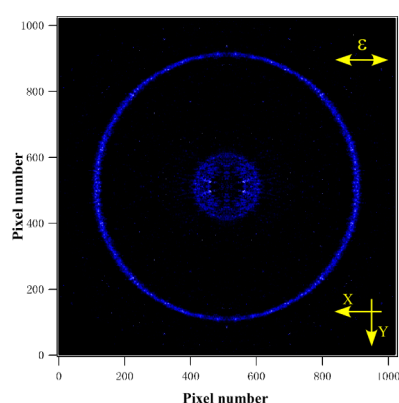

Figure 3. TPEPICO 3D time-sliced image of O^+ ions dissociated from the $O_2^+(^2\Sigma_u^-,v^+=0)$ state at 20.353 eV; (a) the raw image and (b) the modified image.
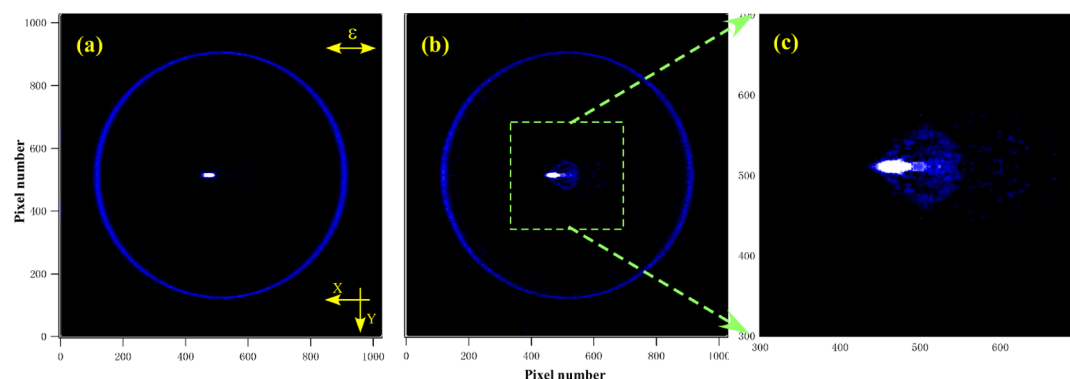
Figure 4. The raw TPEPICO 3D time-sliced image of O$^+$ fragments dissociated from (a) O$_2^+$(B$^2\Sigma_g^-$,v$^+$=3) and (b) O$_2^+$($^2\Sigma_u^-$,v$^+$=4) states; (c) the magnified center part of (b).

O$^+$ produced in the DPI process of O$_2$ at 20.817 eV is presented in Figure 5. As the photon energy increased, the

Figure 5. The modified TPEPICO 3D time-sliced image of O$^+$ produced in the DPI process of O$_2$ at 20.817 eV.

center doughnut in images gradually changed to a ring in Figure 5. Moreover, both diameters of the inner and outer rings increased with the photon energy. As described above, the O$_2^+$($^2\Sigma_u^-$,v$^+$=5) and O$_2^+$(B$^2\Sigma_g^-$,v$^+$=4) ions are produced simultaneously at 20.817 eV. Therefore, the image in Figure 5 should originate from dissociation of O$_2^+$ in both $^2\Sigma_u^-$(v$^+$=5) and B$^2\Sigma_g^-$(v$^+$=4) states. An estimation of branching ratios will be shown in section 3.4.

From the images in Figures 3−5, the speed distribution of O$^+$ fragments dissociated from vibrational state-selected O$_2^+$($^2\Sigma_u^-$) ions can be derived by integrating the intensity of the image over the angle. Taking the dissociation limits for the O$^+$(^{4}S) +

O(^{3}P) and O$^+$(^{4}S) + O(^{1}D) channels, the speed of O$^+$ fragments can be calculated as well based on energy and momentum conservations in dissociation. Therefore, both experimental and calculated speeds of O$^+$ fragment ions are obtained and summarized in Table 1. Obviously, the experimental and calculated data agree very well, and the errors of less than 23 m·s^{-1} mainly come from the energy uncertainty of the beamline.

3.3. Predissociation Mechanism of O$_2^+$($^2\Sigma_u^-$). In the previous experimental investigation,[17] the appearance of the inner doughnut in images oscillated with the photon energy, so that it appeared for B$^2\Sigma_g^-$(v$^+$=4,6) states but disappeared for the B$^2\Sigma_g^-$(v$^+$=5) state. On the basis of the calculated potential energy curves of O$_2^+$, the second dissociation pathway for the B$^2\Sigma_g^-$ state was performed by crossing between the 2$^4\Pi_g$ and B$^2\Sigma_g^-$ states at an energy around the B$^2\Sigma_g^-$(v$^+$=6) level.[34] Therefore, a potential reason was suggested to explain the amazing opening of the O$^+$(^{4}S) + O(^{1}D) channel at the B$^2\Sigma_g^-$(v$^+$=4) level, that the quasi-resonance concomitant $^2\Sigma_u^-$(v$^+$=5) state can predissociate to O$^+$(^{4}S) and O(^{1}D) fragments via the crossing with 2$^4\Pi_u$ states.[17] However, this accidental resonance between the other vibrational states of B$^2\Sigma_g^-$ and $^2\Sigma_u^-$ does not exist. Thus, the second dissociation channel cannot be observed for the B$^2\Sigma_g^-$(v$^+$=5) state until the photon energy is beyond the crossing position between the B$^2\Sigma_g^-$ and 2$^4\Pi_g$ states, for example, at the B$^2\Sigma_g^-$(v$^+$=6) level.

As mentioned above, dissociative mechanisms of the $^2\Sigma_u^-$ and B$^2\Sigma_g^-$ states should be entirely different, although their energies are very close. Because dissociation limits calculated by Beebe et al.[34] were consistent with the experimental data, their potential energy curves of the low-lying electronic states of O$_2^+$

Table 1. Speeds and Anisotropic Parameters (β) of O$^+$ Fragment Ions Dissociated from Various Vibrational State-Selected O$_2^+$($^2\Sigma_u^-$) Ions^a

			speed of O$^+$ (m/s)		
vibronic level	$h\nu$ (eV)	dissociation channel	exp.	cal.	β
$^2\Sigma_u^-$,v$^+$=0	20.353	O$^+$(^{4}S) + O(^{3}P)	3117 ± 10	3126	0.40 ± 0.07
$^2\Sigma_u^-$,v$^+$=3	20.638	O$^+$(^{4}S) + O(^{3}P)	3381 ± 10	3389	0.41 ± 0.08
$^2\Sigma_u^-$,v$^+$=4	20.727	O$^+$(^{4}S) + O(^{3}P)	3453 ± 10	3468	0.44 ± 0.07
		O$^+$(^{4}S) + O(^{1}D)^b	427 ± 10	404	
$^2\Sigma_u^-$,v$^+$=5	20.817	O$^+$(^{4}S) + O(^{3}P)^c	3552 ± 10	3545	0.18 ± 0.09
		O$^+$(^{4}S) + O(^{1}D)	853 ± 10	840	

^{a}The v$^+$ = 1,2 levels of the $^2\Sigma_u^-$ state overlap with the B$^2\Sigma_g^-$(v$^+$=1,2) states. ^{b}The image intensity of the O$^+$(^{4}S) + O(^{1}D) channel is too weak to calculate β. ^{c}Partial contributions are coming from the predissociation of O$_2^+$(B$^2\Sigma_g^-$,v$^+$=4) ions.
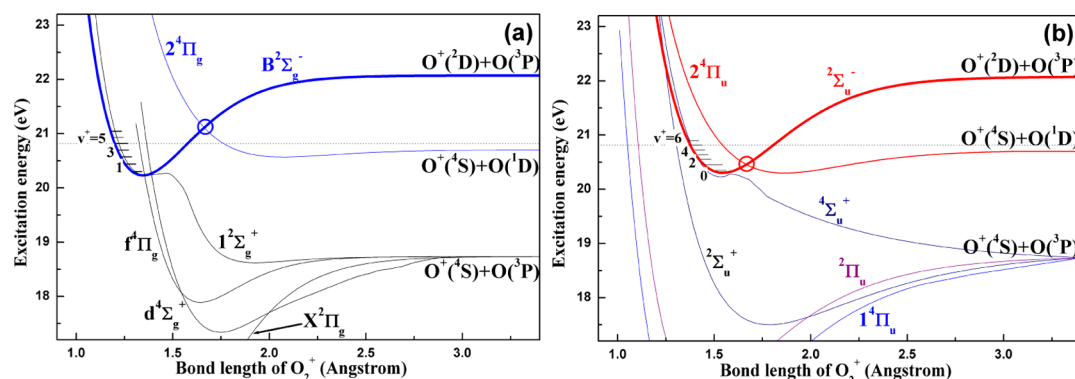
Figure 6. Potential energy curves of O_2^+ ions from ref 34; low-lying electronic states with (a) gerade symmertry and (b) ungerade symmetry. The dotted line represents the excitation energy of 20.817 eV.

were generally quoted to discuss the corresponding predissociation mechanism. Here, our discussion is also based on Beebe et al.'s curves,[34] which are shown in Figure 6.

For the $^2\Sigma_u^-(v^+=0-3)$ vibrational states, only $O^+(^4S)$ and $O(^3P)$ fragments can be produced due to energy restriction. As shown in Figure 6b, the $^2\Sigma_u^-$ and repulsive $^4\Sigma_u^+$ states nearly overlap, especially in the Franck−Condon region. Thus, the strong interaction between them can cause $O_2^+(^2\Sigma_u^-)$ ions to efficiently predissociate to produce $O^+(^4S)$ and $O(^3P)$ fragments. In addition, the nearby $^2\Sigma_u^+$ state is also a possible candidate to make $O_2^+(^2\Sigma_u^-)$ ions dissociate along the $O^+(^4S)$ + $O(^3P)$ channel because their interaction cannot be ignored in the Franck−Condon region.

In the present excitation energy range, only $2^4\Pi_g$ and $2^4\Pi_u$ states correlate adiabatically with the dissociation limit of $O^+(^4S)$ + $O(^1D)$, as shown in Figure 6. Therefore, the unique mechanism to produce $O^+(^4S)$ and $O(^1D)$ fragments from the $O_2^+(^2\Sigma_u^-, v^+=4-6)$ ions is via the crossing between $^2\Sigma_u^-$ and nearby $2^4\Pi_u$ states (noted as the red circle in Figure 6b). Because the energy of the crossing point between $^2\Sigma_u^-$ and $2^4\Pi_u$ states is lower than the dissociation limit of $O^+(^4S)$ + $O(^1D)$, the inner doughnut in O^+ images can be observed once the $O_2^+(^2\Sigma_u^-, v^+=4-6)$ ions are produced. Similarly, predissociation of $O_2^+(B^2\Sigma_g^-, v^+)$ ions along the $O^+(^4S)$ + $O(^1D)$ channel is via the crossing with the $2^4\Pi_g$ state (noted as the blue circle in Figure 6a). However, the $O^+(^4S)$ + $O(^1D)$ products cannot be detected for the $O_2^+(B^2\Sigma_g^-, v^+=4,5)$ ions because the energy of the crossing point with the $2^4\Pi_g$ state is still higher than them, as shown in Figure 6a, although their energies have exceeded the $O^+(^4S)$ + $O(^1D)$ limit.

From the coincidence images in Figures 3−5, angular distributions of O^+ can be derived by integrating over a proper range of speeds at each angle, and then, the anisotropy parameter β can be obtained consequently by fitting the angular distribution.[38] All β values are listed in Table 1, where those for the $O^+(^4S)$ + $O(^1D)$ channel cannot be obtained because the inner doughnuts in Figures 4b and 5 do not exactly reflect the 3D distribution of the O^+ fragment. The β values for the $^2\Sigma_u^-$ state are kept at ∼0.4 for the lowest dissociation channel, except the $v^+ = 5$ state of $^2\Sigma_u^-$, which is seriously influenced by the quasi-resonant $v^+ = 4$ state of $B^2\Sigma_g^-$. According to the fact that the β values of dissociation of the $B^2\Sigma_g^-$ state are near 0.25,[17] predissociation of the $^2\Sigma_u^-$ state along the lowest channel is faster than that of the $B^2\Sigma_g^-$ state.

3.4. Branching Ratio at 20.817 eV. For DPI of O_2 at 20.817 eV, both $^2\Sigma_u^-(v^+=5)$ and $B^2\Sigma_g^-(v^+=4)$ vibrational states are produced simultaneously in experiments. An interesting

keypoint is to estimate their contributions to the observed $O^+(^4S)$ fragments. As mentioned above, both $^2\Sigma_u^-$ and $B^2\Sigma_g^-$ states can predissociate to $O^+(^4S)$ and $O(^3P)$ fragments and contribute to the outer ring in the image of Figure 5. On the contrary, only dissociation of the $^2\Sigma_u^-(v^+=5)$ state can produce O^+ along the second dissociation pathway and contribute to the inner doughnut in the image. Therefore, contribution of the $^2\Sigma_u^-(v^+=5)$ state to the first channel (the outer ring in the image) can be derived from the intensity of the inner doughnut.

However, the observed inner doughnut in images cannot exactly reflect the 3D distribution of O^+ due to limitation of the 60 ns mass gate. Thus, we prefer to calculate the branching ratios by fitting the TOF profiles of O^+ in Figure 2. For the $^2\Sigma_u^-(v^+=6)$ state, the branching ratio of two dissociation channels, $[O^+ + O(^1D)]/[O^+ + O(^3P)]$, is around 10%. Supposing that the branching ratios do not change dramatically for adjacent vibronic levels of the same $^2\Sigma_u^-$ state, it should be about 10% as well for $^2\Sigma_u^-(v^+=5)$. By fitting the TOF profile of O^+ in Figure 2c, the ratio of O^+ ions from the $O^+(^4S)$ + $O(^1D)$ channel is only 6%. Therefore, the ratios of contribution to the outer ring in the image from the $O_2^+(^2\Sigma_u^-, v^+=5)$ ions should be ∼60%, and the other O^+ fragments with the higher speed (the outer ring) are coming from dissociation of $O_2^+(B^2\Sigma_g^-, v^+=4)$ ions. Near 34% of the O^+ intensity is therefore coming from dissociation of the $O_2^+(B^2\Sigma_g^-, v^+=4)$ ions at 20.817 eV.

4. CONCLUSIONS

Using synchrotron radiation as a light source, DPI of O_2 via the $^2\Sigma_u^-$ ionic state was investigated by the method of TPEPICO velocity imaging. TPES of O_2 in the excitation energy range of 20.2−21.1 eV was measured. According to the previous spectral assignments, two series of vibrational bands are respectively assigned as the strong $B^2\Sigma_g^-(v^+=0-6)$ and the weak concomitant $^2\Sigma_u^-(v^+=0-6)$ vibrational states.

In the coincident mass spectra, the TOF profile of the O^+ fragment is observed and obviously broadened, while no TOF peak for O_2^+ ions is observed. Thus, all $^2\Sigma_u^-$ vibrational states are completely predissociative, like the nearby $B^2\Sigma_g^-$ ionic state. Subsequently, TPEPICO 3D time-sliced images of O^+ dissociated from vibrational state-selected $O_2^+(^2\Sigma_u^-, v^+)$ ions were recorded. For the $^2\Sigma_u^-(v^+=0-3)$ vibrational states, only $O^+(^4S)$ and $O(^3P)$ fragments from the lowest dissociation channel were observed and contributed to an outer ring in the image. Once the photon energy is slightly increased to the $^2\Sigma_u^-(v^+=4)$ vibronic level at 20.727 eV (just above the second dissociation limit), a new concentric doughnut appears in the

image, indicating that the second $O^+(^4S) + O(^1D)$ dissociation channel is observed indeed. In addition, a near-isotropic distribution of O^+ is presented in all images, and thus, dissociation lifetimes of all vibronic levels of $^2\Sigma_u^-$ are longer than that of molecular rotation.

At 20.817 eV, both $^2\Sigma_u^-(v^+=5)$ and $B^2\Sigma_g^-(v^+=4)$ vibrational states are produced simultaneously. Interestingly, only dissociation of the $^2\Sigma_u^-(v^+=5)$ state can produce O^+ along the second dissociation pathway, while both $^2\Sigma_u^-(v^+=5)$ and $B^2\Sigma_g^-(v^+=4)$ states can predissociate to $O^+(^4S)$ and $O(^3P)$ fragments. However, the recorded inner doughnut in the image cannot exactly reflect the 3D distribution of O^+ due to the limitation of the 60 ns mass gate. Therefore, the branching ratio for the $B^2\Sigma_g^-(v^+=4)$ state at 20.817 eV can be estimated as 34% by fitting the TOF profiles of O^+.

With the aid of the calculated potential energy curves of O_2^+, the dissociative mechanism for the $^2\Sigma_u^-(v^+)$ state is proposed. The strong interaction between $^2\Sigma_u^-$ and repulsive $^4\Sigma_u^+$ states can cause $O_2^+(^2\Sigma_u^-)$ ions to efficiently dissociate to produce $O^+(^4S)$ and $O(^3P)$ fragments. Moreover, the nearby $^2\Sigma_u^+$ state is also a possible candidate to make $O_2^+(^2\Sigma_u^-)$ ions dissociate along the lowest channel. The unique mechanism to produce $O^+(^4S)$ and $O(^1D)$ fragments from the $O_2^+(^2\Sigma_u^-,v^+=4-6)$ ions is via the crossing between $^2\Sigma_u^-$ and nearby $2^4\Pi_u$ states.

As a typical ionic optical dark state, it is difficult to investigate dissociation dynamics of $^2\Sigma_u^-$ via photoexcitation from the ionic ground state of gerade symmetry. However, it can be produced in TPEPICO experiments, and direct experimental evidence for DPI of O_2 via this optical dark state is shown here. Therefore, the TPEPICO measurement is a powerful tool indeed to investigate more details and mysteries of molecular ions.

■ AUTHOR INFORMATION

Corresponding Author
*Tel: +86-551-3600031. E-mail: xzhou@ustc.edu.cn.

Notes
The authors declare no competing financial interest.

■ ACKNOWLEDGMENTS

■ REFERENCES

(1) Baer, T. State selection by photoion−photoelectron coincidence. In *Gas Phase Ion Chemistry*; Bowers, M. T., Ed.; Academic Press: New York, 1979; pp 153−196.

(2) Baer, T. Vacuum UV photophysics and photoionization spectroscopy. *Annu. Rev. Phys. Chem.* **1989**, *40*, 637−669.

(3) Ng, C. Y. Vacuum ultraviolet spectroscopy and chemistry by photoionization and photoelectron methods. *Annu. Rev. Phys. Chem.* **2002**, *53*, 101−140.

(4) Borkar, S.; Sztaray, B.; Bodi, A. Dissociative photoionization mechanism of methanol isotopologues (CH_3OH, CD_3OH, CH_3OD and CD_3OD) by iPEPICO: energetics, statistical and non-statistical kinetics and isotope effects. *Phys. Chem. Chem. Phys.* **2011**, *13* (28), 13009−13020.

(5) Gaie-Levrel, F.; Garcia, G. A.; Schwell, M.; Nahon, L. VUV state-selected photoionization of thermally-desorbed biomolecules by coupling an aerosol source to an imaging photoelectron/photoion coincidence spectrometer: case of the amino acids tryptophan and phenylalanine. *Phys. Chem. Chem. Phys.* **2011**, *13* (15), 6993−7005.

(6) Holland, D. M. P.; Shaw, D. A.; Sumner, I.; Hayes, M. A.; Mackie, R. A.; Wannberg, B.; Shpinkova, L. G.; Rennie, E. E.; Cooper, L.; Johnson, C. A. F.; et al. The design and performance of a threshold-photoelectron−photoion coincidence spectrometer for the study of unimolecular decomposition in polyatomic ions. *Nucl. Instrum. Methods Phys. Res., Sect. B* **2001**, *179* (3), 436−454.

(7) Howle, C. R.; Collins, D. J.; Tuckett, R. P.; Malins, A. E. R. Threshold photoelectron−photoion coincidence spectroscopy study of $CHCl_2F^+$, $CHClF_2^+$ and CH_2ClF^+: Steric influence of the chlorine, uorine and hydrogen atoms. *Phys. Chem. Chem. Phys.* **2005**, *7* (11), 2287−2297.

(8) Garcia, G. A.; Soldi-Lose, H.; Nahon, L. A versatile electron−ion coincidence spectrometer for photoelectron momentum imaging and threshold spectroscopy on mass selected ions using synchrotron radiation. *Rev. Sci. Instrum.* **2009**, *80* (2), 023102−023113.

(9) Bodi, A.; Johnson, M.; Gerber, T.; Gengeliczki, Z.; Sztaray, B.; Baer, T. Imaging photoelectron photoion coincidence spectroscopy with velocity focusing electron optics. *Rev. Sci. Instrum.* **2009**, *80* (3), 034101−034107.

(10) Baer, T.; Dunbar, R. C. Ion spectroscopy: where did it come from; where is it now; and where is it going? *J. Am. Soc. Mass. Spectrom.* **2010**, *21* (5), 681−693.

(11) Tang, X. F.; Zhou, X. G.; Niu, M. L.; Liu, S. L.; Sun, J. D.; Shan, X. B.; Liu, F. Y.; Sheng, L. S. A threshold photoelectron−photoion coincidence spectrometer with double velocity imaging using synchrotron radiation. *Rev. Sci. Instrum.* **2009**, *80* (11), 113101−113110.

(12) Tang, X. F.; Niu, M. L.; Zhou, X. G.; Liu, S. L. Spectroscopic studies of molecular ions and their dissociation dynamics by the threshold photoelectron-photoion coincidence. *Acta Phys. Sin.* **2010**, *59* (10), 6940−6947.

(13) Zhen, C.; Tang, X. F.; Zhou, X. G.; Liu, S. L. Application and improvement in the ion velocity imaging of threshold photoelectron−photoion coincidence measurements. *Acta Phys. Chim. Sin.* **2011**, *27* (7), 1574−1578.

(14) Eppink, A.; Parker, D. H. Velocity map imaging of ions and electrons using electrostatic lenses: Application in photoelectron and photofragment ion imaging of molecular oxygen. *Rev. Sci. Instrum.* **1997**, *68* (9), 3477−3484.

(15) Ashfold, M. N. R.; Nahler, N. H.; Orr-Ewing, A. J.; Vieuxmaire, O. P. J.; Toomes, R. L.; Kitsopoulos, T. N.; Garcia, I. A.; Chestakov, D. A.; Wu, S. M.; Parker, D. H. Imaging the dynamics of gas phase reactions. *Phys. Chem. Chem. Phys.* **2006**, *8* (1), 26−53.

(16) Tang, X. F.; Zhou, X. G.; Niu, M. L.; Liu, S. L.; Liu, F. Y.; Shan, X. B.; Sheng, L. S. NO^+ formation pathways in dissociation of N_2O^+ ions at the $C^2\Sigma^+$ state revealed from threshold photoelectron−photoion coincidence velocity imaging. *J. Chem. Phys.* **2011**, *134* (5), 054312−054321.

(17) Tang, X. F.; Zhou, X. G.; Niu, M. L.; Liu, S. L.; Sheng, L. S. Dissociation of vibrational state-selected O_2^+ ions in the $B^2\Sigma_g^-$ state using threshold photoelectron−photoion coincidence velocity imaging. *J. Phys. Chem. A* **2011**, *115* (24), 6339−6346.

(18) Tang, X. F.; Zhou, X. G.; Wu, M. M.; Liu, S. L.; Liu, F. Y.; Shan, X. B.; Sheng, L. S. Dissociative photoionization of methyl chloride studied with threshold photoelectron−photoion coincidence velocity imaging. *J. Chem. Phys.* **2012**, *136* (3), 034304−034311.

(19) Wu, M. M.; Tang, X. F.; Niu, M. L.; Zhou, X. G.; Dai, J. H.; Liu, S. L. Ionization and dissociation of methyl chloride in an excitation energy range of 13−17 eV. *Acta Phys. Chim. Sin.* **2011**, *27* (12), 2749−2754.

(20) Niu, M. L.; Song, L.; Tang, X. F.; Zhou, X. G.; Liu, S. L.; Liu, F. Y.; Shan, X. B.; Sheng, L. S. Dissociation dynamics of O^+ formation channels from vibrational state-selected NO_2^+ at e^3B_2 State. *Acta Phys. Chim. Sin.* **2011**, *27* (8), 1797−1802.

(21) Edqvist, O.; Lindholm, E.; Selin, L. E.; Asbrink, L. On the photoelectron spectrum of O_2. *Phys. Scr.* **1970**, *1* (1), 25−30.

(22) Tanaka, T.; Yoshii, H.; Morioka, Y.; Hayaishi, T.; Ito, K.; Hall, R. I. High-resolution threshold photoelectron spectra of molecular oxygen in the 18−24 eV region. *J. Chem. Phys.* **1998**, *108* (15), 6240−6248.

(23) Merkt, F.; Guyon, P. M.; Hepburn, J. High-resolution threshold photoelectron spectrum of molecular oxygen. *Chem. Phys.* **1993**, *173* (3), 479−489.

(24) Merkt, F.; Guyon, P. M. Threshold photoelectron spectrum of molecular oxygen in the region of the $B^2\Sigma_g^- \leftarrow X^3\Sigma_g^-$ transition. *J. Phys. Chem.* **1995**, *99* (43), 15775−15778.

(25) Ellis, K.; Hall, R. I.; Avaldi, L.; Dawber, G.; McConkey, A.; Andric, L.; King, G. C. High-resolution threshold photoelectron and photoion spectroscopy of oxygen in the 12−50 eV photon range. *J. Phys. B: At., Mol. Opt. Phys.* **1994**, *27* (15), 3415−3426.

(26) Evans, M.; Stimson, S.; Ng, C. Y.; Hsu, C. W.; Jarvis, G. K. Rotationally resolved pulsed field ionization photoelectron study of $O_2^+(B^2\Sigma_g^-, {}^2\Sigma_u^-; v^+ = 0−7)$ at 20.2−21.3 eV. *J. Chem. Phys.* **1999**, *110* (1), 315−327.

(27) Bombach, R.; Schmelzer, A.; Stadelmann, J. P. The predissociation of molecular oxygen cations $O_2^+(B^2\Sigma_g^-)$. *Chem. Phys.* **1981**, *61* (1−2), 215−219.

(28) Blyth, R. G. C.; Powis, I.; Danby, C. J. Competing predissociation of $O_2^+(B^2\Sigma_g^-)$. *Chem. Phys. Lett.* **1981**, *84* (2), 272−275.

(29) Bombach, R.; Schmelzer, A.; Stadelmann, J. P. Predissociation of the molecular oxygen cations ${}^{16}O_2^+$ and ${}^{18}O_2^+$ studied by photoelectron photoion coincidence spectroscopy. *Int. J. Mass Spectrom. Ion Processes* **1982**, *43* (2−3), 211−225.

(30) Guyon, P. M.; Baer, T.; Ferreira, L. F. A.; Nenner, I.; Tabchefouhaile, A.; Botter, R.; Govers, T. R. Observation of dissociative states of O_2^+ by threshold photoelectron−photoion coincidence. *J. Phys. B: At., Mol. Opt. Phys.* **1978**, *11* (5), L141−L144.

(31) Akahori, T.; Morioka, Y.; Watanabe, M.; Hayaishi, T.; Ito, K.; Nakamura, M. Dissociation processes of O_2 in the VUV region 500−700A. *J. Phys. B: At., Mol. Opt. Phys.* **1985**, *18* (11), 2219−2229.

(32) Richard-Viard, M.; Dutuit, O.; Lavollee, M.; Govers, T.; Guyon, P. M.; Durup, J. O_2^+ ions dissociation studied by threshold photoelectron photoion coincidence method. *J. Chem. Phys.* **1985**, *82* (9), 4054−4063.

(33) Lafosse, A.; Brenot, J. C.; Golovin, A. V.; Guyon, P. M.; Hoejrup, K.; Houver, J. C.; Lebech, M.; Dowek, D. Vector correlations in dissociative photoionization of O_2 in the 20−28 eV range. I. Electron−ion kinetic energy correlations. *J. Chem. Phys.* **2001**, *114* (15), 6605−6617.

(34) Beebe, N. H. F.; Thulstrup, E. W.; Andersen, A. Configuration interaction calculation of low-lying electronic states of O_2, O_2^+, and O_2^{2+}. *J. Chem. Phys.* **1976**, *64* (5), 2080−2093.

(35) Marian, C. M.; Marian, R.; Peyerimhoff, S. D.; Hess, B. A.; Buenker, R. J.; Seger, G. Ab initio CI calculation of O_2^+ predissociation phenomena induced by a spin orbit coupling mechanism. *Mol. Phys.* **1982**, *46* (4), 779−810.

(36) Wang, S. S.; Kong, R. H.; Shan, X. B.; Zhang, Y. W.; Sheng, L. S.; Wang, Z. Y.; Hao, L. Q.; Zhou, S. K. Performance of the atomic and molecular physics beamline at the National Synchrotron Radiation Laboratory. *J. Synchrotron Radiat.* **2006**, *13* (6), 415−420.

(37) Townsend, D.; Minitti, M. P.; Suits, A. G. Direct current slice imaging. *Rev. Sci. Instrum.* **2003**, *74* (4), 2530−2539.

(38) Zare, R. N. Photoejection dynamics. *Mol. Photochem.* **1972**, *4*, 1−37.